Reactive–diffusion epidemic model on human mobility networks: Analysis and applications to COVID-19 in China

Ruqi Li [a], Yurong Song [b],*, Haiyan Wang [c], Guo-Ping Jiang [b], Min Xiao [b]

[a] School of Computer Science, Nanjing University of Posts and Telecommunications, Nanjing 210003, China
[b] College of Automation and College of Artificial Intelligence, Nanjing University of Posts and Telecommunications, Nanjing 210023, China
[c] School of Mathematical and Natural Sciences, Arizona State University, Phoenix, AZ 85069, USA

ABSTRACT

The complex dynamics of human mobility, combined with sporadic cases of local outbreaks, make assessing the impact of large-scale social distancing on COVID-19 propagation in China a challenge. In this paper, with the travel big dataset supported by Baidu migration platform, we develop a reactive–diffusion epidemic model on human mobility networks to characterize the spatio-temporal propagation of COVID-19, and a novel time-dependent function is incorporated into the model to describe the effects of human intervention. By applying the system control theory, we discuss both constant and time-varying threshold behavior of proposed model. In the context of population mobility-mediated epidemics in China, we explore the transmission patterns of COVID-19 in city clusters. The results suggest that human intervention significantly inhibits the high correlation between population mobility and infection cases. Furthermore, by simulating different population flow scenarios, we reveal spatial diffusion phenomenon of cases from cities with high infection density to cities with low infection density. Finally, our model exhibits acceptable prediction performance using actual case data. The localized analytical results verify the ability of the PDE model to correctly describe the epidemic propagation and provide new insights for controlling the spread of COVID-19.

© 2022 Elsevier B.V. All rights reserved.

1. Introduction

Infectious diseases spread geographically on a large scale in a short period of time, affecting the lives of people around the world, such as the current COVID-19 pneumonia [1]. While the efficiency, speed, and reach of modern transports have strengthened the connectivity between individuals, it has also increased the spread risk of highly virulent emergent pathogens [2,3]. In order to restrict the spread of SARS-CoV-2, vaccination is being actively promoted in many countries [4]. On the other hand, non-pharmaceutical interventions are being implemented, such as travel restrictions, physical distancing and wearing masks [5,6]. However, due to the continuous variation of SARS-CoV-2 [7], research of contagion mechanisms and mitigation strategies has become an urgent and serious subject with theoretical and practical significance.

Mathematical modeling has become an indispensable way for predicting the evolution of pandemics and supporting government decision-making. Since the seminal epidemic model of Kermack and McKendrick in the early 20th century [8],

a large number of novel compartmental models involving specific disease types and realistic diffusion mechanisms has been proposed [9–13]. Wang et al. [9] investigated a diffusive cholera model with general incidence functions. Here, it was shown that Cholera cannot be controlled only by limiting the movement of host individuals. Rizzo et al. [11] discussed a realistic Ebola model to describe EVD spreading based on activity driven networks, and reproduced the dynamics of the 2014–2015 Ebola outbreak in Liberia. Huang et al. [12] developed a mechanism-based HIV dynamic model in which the inhibition rate involves drug concentration, adherence, and drug susceptibility. A hierarchical Bayesian method was utilized to estimate the dynamic parameters in Ref. [12].

Besides, in response to the global epidemic of COVID-19, a variety of COVID-19 epidemic models are attracting widespread attention [14–19]. Jia et al. [15] found that there was a significant correlation between local population mobility and COVID-19 cases, and established a risk source model that leverages population flow data. This research identified high-transmission-risk locales at an early stage in China. Yang et al. [16] modified the standard Susceptible– Expose–Infectious–Removed (SEIR) model by introducing the move-in and move-out parameters, and compared the deep learning algorithm LSTM for predicting COVID-19 epidemic trends. Wang et al. [17] established a delayed differential system of equations considering the characteristics of the COVID-19 epidemic phenomenon. The existence of Hopf bifurcations associated with two equilibria were discussed in their work. Epidemic propagation is often associated with the age of individuals [20,21]. Prem et al. [22] divided different contact patterns according to age structure to simulate the persistent trajectory of the COVID-19 under control and deregulation measures, and the results showed the impact of returning to work at different stages of the underlying epidemic.

In recent years, some studies have combined mathematical modeling with complex networks for understanding propagating phenomena in biology, sociology and physics, in which the nodes represent individuals or clusters, and the edges mimic the interactions among them. Assuming that the population is mixed homogeneously, Hethcote [23] estimated the basic reproduction number and the model parameters of various diseases including measles in Niger and pertussis in the United States. Utilizing small-world and random networks, Yang [24] discussed the spreading of diseases in the process of evolution on multilayer homogeneous networks. Unlike classical epidemic models, it is significant and necessary to take contact heterogeneity into account when modeling diffusion process on the complex networks. Feng et al. [25] put forward a discrete-time Markov chain method to model SIR epidemic dynamics in heterogeneous networks with residences, common places and different kinds of connections. Considering only the extreme simplification of two degrees, a low degree close to the mean degree and a high degree about ten times the mean degree, Rafo et al. [26] discussed main features of disease dynamics in scale-free networks. By introducing feedback mechanism, Li et al. [27] applied the mean field theory to analyze the stability and control strategies of modified SIRS epidemic model on adaptive scale-free networks.

Most prior research on network-driven epidemic model have focused on the understanding of artificial network structure, which may not accurately and completely express the attribute information of nodes and links, clustering and multi-level structure information in real networks. Several works have studied the key properties of propagation dynamics by using ordinary differential equation (ODE) models, which only support the spread of epidemics along the temporal dimension. However, little attempt has been given on understanding and modeling real network-driven contagion phenomena in both temporal and spatial dimensions based on partial differential equation (PDE). Specifically, we are interested in answering the spatio-temporal diffusion problems: after the initial outbreak of an epidemic, where does the pathogen invade first? What is the number of infected cases? How does population mobility affect the trans-regional spread of the epidemic?

In fact, PDEs have been proved to be a suitable modeling tool for establishing spatio-temporal disease dynamics systems. Under the condition of spatial continuity, they have addressed questions such as spatial heterogeneity [9], nonlinear infection mechanism [28,29] and spatial diffusivity [30]. However, in reality, due to the complexity and incoherence of human movement patterns, determining how the natural integration of PDEs model and real systems is still the main objective.

Historically, using friendship hops to define a spatial distance in social networks, Wang et al. [31,32] developed a PDE, a linear diffusive model to characterize the spatiotemporal information propagation. Our previous work had also attempted to model how the disease spreads taking into account temporal and spatial effects based on PDEs. In [33], we only considered the one-hop traffic relationship to define a distance in the spread of the disease. Despite the simplicity of the above link topology, these models permit the capture of the lower-order connectivity and boundary information from real systems at the level of individual nodes and edges. It remains largely unknown how high-order organizational characteristics at the level of small network subgraphs affect the spread of epidemics in complex networks.

In this paper, we propose a network-driven PDE epidemic model, and combine the concept of network motif to address this situation. The major contributions in the paper are as follows. First, we utilize anonymous aggregated Baidu Migration Data to develop a human mobility network for Chinese cities, and analyze the geographically complex spatial interaction between regions using the higher-order approach. Second, based on local growth process along time and the global diffusion process along space, we make use of partial differential equations to develop a network-driven epidemic model for describing the spatio-temporal spread of the disease, into which a time-dependent function is incorporated to characterize human intervention. Third, since the time-dependent function changes the type of system, we will discuss the stability of autonomous and non-autonomous systems respectively. Finally, we will demonstrate the validity of our model by exploring how COVID-19 spread changed (i.e., the epidemic arrival time, infection size and infection duration in affected locations) under different interventions, mobility intensity as well as real epidemiological data.
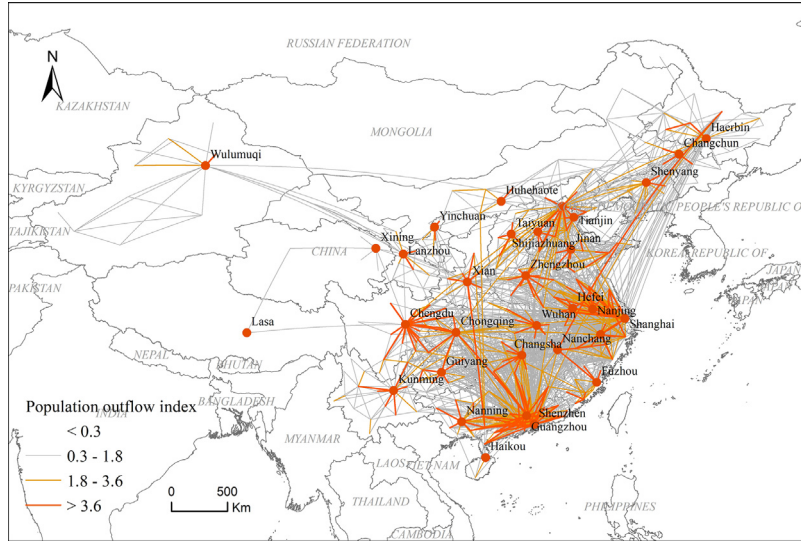
Fig. 1. Grading map of population outflow in mainland China as of the eve of the Spring Festival.

The remainder of this paper is organized as follows. In Section 2, a modeling approach for network-driven epidemic model is described explicitly. In Section 3, the model-related results are discussed, including a priori bound of the solution, the existence of disease equilibrium points and the stability of PDE model. In human mobility network environments with different interventions, several numerical simulations are presented in Section 4, to illustrate the propagation feature of COVID-19 pneumonia. Finally, conclusions and future work are discussed in Section 5.

2. Network-driven PDE model

2.1. Data sources

In this paper, the population mobility data is provided by 2020 *ChunYun* section of Baidu Migration Platform (https://qianxi.baidu.com). We use two kinds of raw data, one is the daily population outflow index of city i from January 10, 2020 to January 24, 2020, and the other is the proportion of daily outflow index from city i to city j from January 10, 2020 to January 24, 2020.

To facilitate the application of the human mobility network in the dynamic system, the data processing process is as follows: first, by multiplying the daily outflow index of city i by the proportion of daily outflow index from city i to destination j, we obtain the daily population outflow index between pairs of cities. Second, the daily population outflow index from city i to city j is added to get the final population outflow index (POI) between pairs of cities, as shown in Fig. 1. Third, by normalizing the final population outflow index, we establish a bi-directional graph $P = (P_{ij})$ with $0 \leq P_{ij} \leq 1$ to characterize the pattern of human mobility in China, in which nodes represent cities and weighted-directed links P_{ij} quantify the fraction of the population outflow index from city i to city j. Mathematically the 336*336 asymmetrical matrices can be expressed as follows:

$$P_{ij} = \begin{bmatrix} 0 & P_{12} & \cdots & P_{1(n-1)} & P_{1n} \\ P_{21} & 0 & \cdots & P_{2(n-1)} & P_{2n} \\ \vdots & \vdots & \vdots & \vdots & \vdots \\ P_{(n-1)1} & P_{(n-2)2} & \cdots & 0 & P_{(n-1)n} \\ P_{n1} & P_{n2} & \cdots & P_{n(n-1)} & 0 \end{bmatrix}. \tag{1}$$

In general, hundreds of millions of people would complete migration of the Spring Festival holidays on the eve of the Lunar New Year on January 24, 2020 [34]. This is helpful in assessing specific human mobility patterns by using the characteristics of a larger population instead of random and irregular individuals. Fig. 1 shows the grading map of population outflow as of the eve of the Spring Festival. It can be clearly seen that there is close connectivity among metropolises. In addition, cluster structure is obviously revealed due to the massive diversion of the metropolis to the surrounding neighboring cities.
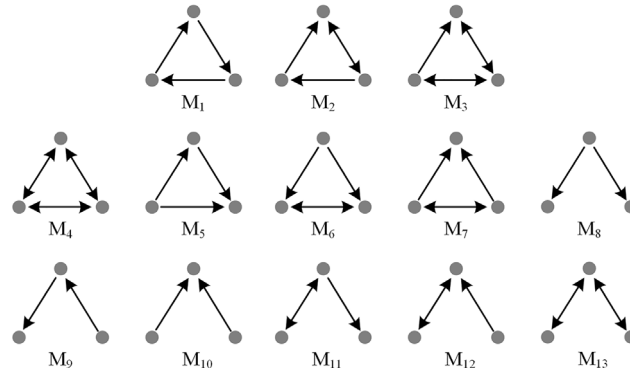
Fig. 2. Three-node directed motifs.

2.2. Clustering and embedding

Using higher-order organizations of complex networks as the basic components of complex network can help us mine the hidden language of complex systems. Small network subgraphs, that is, network motifs, are the most common higher-order organization of complex networks [35,36]. Specifically, three-node directed motifs (see Fig. 2) appear frequently in networks [37]. For example, motifs (M_4, M_5, or M_{13}) are used as the basic unit of the airport network, motif M_7 is the structural hub of the brain, and motifs (M_5, M_6, or M_8) depict differing hierarchical flow between species in the Florida Bay ecosystem food web.

In this paper, the higher order organization, bidirectional motif M_4 in Fig. 2, reflects the COVID-19 diffusion from source to target in city-level network. Combined with the higher-order spectral method in [37], we apply motif M_4 as the basic building block of human mobility network to divide 336 main cities of China into 12 clusters (see Fig. 3 and Supplementary Table 1). The idea of high-order spectral clustering algorithm is as follows: for a given network and the interesting motif, the network is segmented by a hypersurface to obtain two node subsets that complement each other: the complement of S and S. Traversing the hypersurface, we get a target segmentation, which is satisfied with the following requirements: first, the hypersurface avoids segmentation to motif as much as possible; Second, motif falls into a subset of two nodes as much and evenly as possible. The detailed process of the algorithm can be found in [37].

In order to define the spatial distance of disease propagation between clusters, here we get the cluster flux C_x by accumulating the outflow index of the city in each cluster, and arrange the 12 regions $C = \{C_1, C_2, \ldots, C_{12}\}$ based on descending order of cluster flux size (see Supplementary Table 2), where 12 is the maximum distance of disease propagation. Then C_x is embedded at location x based on that x-axis is used as the spatial distance. Further, for each city cluster, one part of newly infected is produced from social interactions with infected people within a cluster, which can be seen as local growth. The other part of newly infected is from other city clusters through global diffusion. As a result, combining the growth process and diffusion process together as shown in Fig. 4, we exploit partial differential equations in spatio-temporal dimension to characterize the spreading dynamic system of COVID-19.

2.3. PDE model

Inspired by the (S, I, R) Kermack–McKendrick equations and recognizing characteristics of COVID-19, in this article we develop a novel reaction–diffusion epidemic model coupled to human mobility networks through a graph Laplacian matrix. The state evolution at node i represents

$$\begin{cases} \dfrac{\partial S_i(t,x)}{\partial t} = \Lambda - \beta \Theta(t, t_c) \dfrac{S_i(t,x)}{N_i} I_i(t,x) - \mu S_i(t,x) + \varepsilon \sum_{k \sim i} P_{ki} (S_k - S_i) \\[2mm] \dfrac{\partial I_i(t,x)}{\partial t} = \beta \Theta(t, t_c) \dfrac{S_i(t,x)}{N_i} I_i(t,x) - (\gamma + \mu) I_i(t,x) + \varepsilon \sum_{k \sim i} P_{ki} (I_k - I_i) \\[2mm] \dfrac{\partial R_i(t,x)}{\partial t} = \gamma I_i(t,x) - \mu R_i(t,x) + \varepsilon \sum_{k \sim i} P_{ki} (R_k - R_i) , i = 1, 2, \ldots, M \end{cases} \quad (2)$$

The meaning of variables are listed in Table 1. Here, we introduce a time-dependent function $\Theta(t, t_c)$ into the model to describe human intervention and it is written in a form

$$\Theta(t, t_c) = \begin{cases} (1 + \exp(t - \frac{t_c}{2}))^{-1}, & with\ intervention, \\ 1, & otherwise, \end{cases} \quad (3)$$
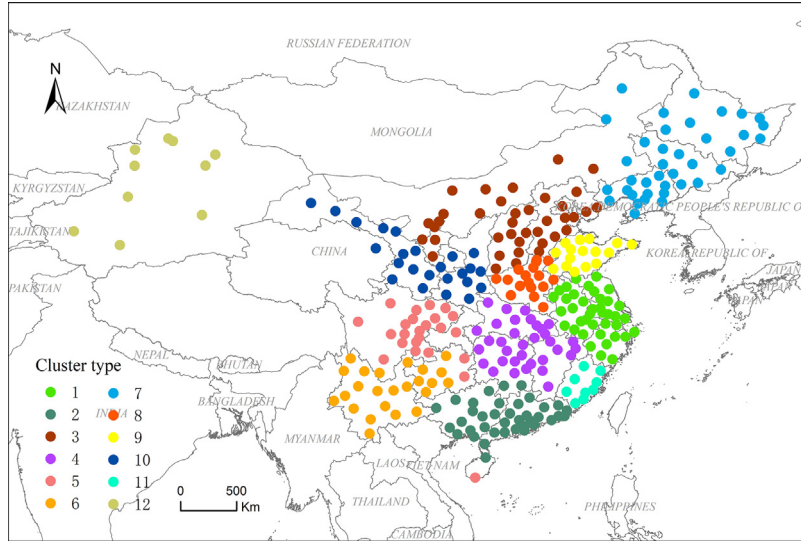
Fig. 3. Twelve clusters obtained by M_4-motif spectral clustering algorithm. The map depicts all locations (nodes) in the model, colored by region.
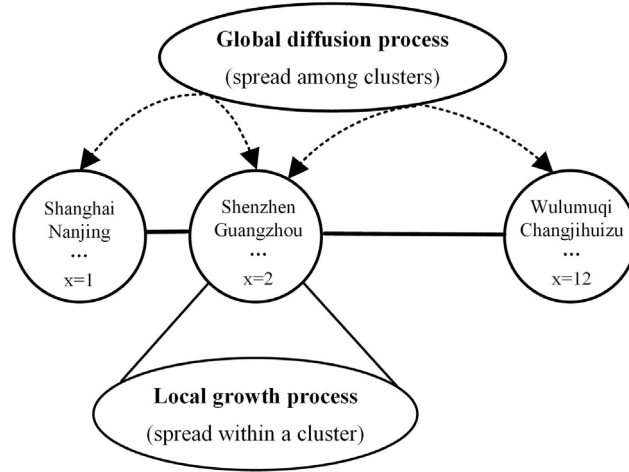

Fig. 4. Embedding of clusters into the x-axis and two spreading processes.

where t_c represents the expected time taken to control the spread of the disease. For any meaningful t_c, the range of function $\Theta(t, t_c)$ is guaranteed to be between 0 and 1. Specifically, given a parameter t_c, the infection incidence rate $\beta\Theta(t, t_c)$ decreases over time t in order to suppress the spread of the disease. Moreover, by adjusting the parameter t_c, this model allows us to examine the effect of human interventions to prevent COVID-19. Actually, a similar form of $\Theta(\cdot)$ has been used to describe human behavior changes such as wearing masks and keeping social distancing to curb epidemics in [38,39].

In a spatially continuous system Eqs. (2) can be rewritten as follow

$$
\begin{cases}
\dfrac{\partial S(t, x)}{\partial t} = \varepsilon\Delta S(t, x) + \Lambda - \beta\Theta(t, t_c)S(t, x)I(t, x) - \mu S(t, x) \\[2mm]
\dfrac{\partial I(t, x)}{\partial t} = \varepsilon\Delta I(t, x) + \beta\Theta(t, t_c)S(t, x)I(t, x) - (\gamma + \mu)I(t, x) \\[2mm]
\dfrac{\partial R(t, x)}{\partial t} = \varepsilon\Delta R(t, x) + \gamma I(t, x) - \mu R(t, x)
\end{cases}
\tag{4}
$$

where $S = S_i/N_i$, $I = I_i/N_i$ and $R = R_i/N_i$ represent the local density of susceptible, infected and removed states, respectively. Δ is the graph Laplacian matrix characterized by the real positive semi-definite matrix, defined as $\Delta_{ki} = -P_{ki}$ if k is incident with i, 0 otherwise; $\Delta_{kk} = \sum_{k \neq i} P_{ki}$.

Table 1
Descriptions of parameters.

Parameter	Description
β	Infection rate of susceptible individuals $S_i(t, x)$
γ	Recovery rate of infected individuals $I_i(t, x)$
Λ	Recruitment rate of susceptible individuals $S_i(t, x)$
μ	Natural death rate of the population
$\Theta(t, t_c)$	Time-dependent function which describes human intervention
P_{ki}	Proportion of population flow with destination k emanating from node i
ε	Average mobility rate
N_i	Population size of node i
M	Number of nodes
$S_i(t, x)$	Number of susceptible individuals with a distance of x at time t
$I_i(t, x)$	Number of infected individuals with a distance of x at time t
$R_i(t, x)$	Number of removed individuals with a distance of x at time t

The model (4) needs to be analyzed with the initial states

$$
\begin{cases}
S(t, x) = S(0, x) \geq 0 \quad and \quad \not\equiv 0, \\
I(t, x) = I(0, x) \geq 0 \quad and \quad \not\equiv 0, \\
R(t, x) = R(0, x) \geq 0 \quad and \quad \not\equiv 0,
\end{cases}
\tag{5}
$$

and the homogeneous Neumann boundary conditions

$$
\frac{\partial S(t, x)}{\partial n} = \frac{\partial I(t, x)}{\partial n} = \frac{\partial R(t, x)}{\partial n} = 0,
\tag{6}
$$

where n is Euclidean space, $t \geq 0$, $x \in \partial\Omega$ and Ω is the spatial domain.

3. Mathematical analysis and simulation

3.1. Positive and boundedness of the system

Theorem 1. *Let $(S(t, x), I(t, x), R(t, x))$ be the solution of the system (4) satisfying initial states (5) and homogeneous Neumann boundary conditions (6), then $(S(t, x), I(t, x), R(t, x))$ is non-negative and uniformly bounded for $t \geq 0$ and $x \in \Omega$. More precisely, we have*

$$
\limsup_{t \to +\infty, x \in \Omega} (S(t, x), I(t, x), R(t, x)) \leq \frac{\Lambda}{\mu}(1, 1, 1).
\tag{7}
$$

Proof. Assume that $t_1 = \sup\{t \geq 0 : S \geq 0, I \geq 0, R \geq 0\} \in [0, t]$. According to the first equation of the system (4), the corresponding non-diffusion equation is

$$
\frac{dS(t)}{dt} + (\beta\Theta I(t) + \mu)S(t) = \Lambda.
\tag{8}
$$

Now integrating both sides of the above equation, we can obtain

$$
S(t_1) \exp\left\{ \int_0^t (\beta\Theta I(u) + \mu)\, du \right\} - S(0) = \int_0^{t_1} \exp\left\{ \int_0^t \Lambda\, (\beta\Theta I(u) + \mu)\, I(u) du \right\} dv,
\tag{9}
$$

and work out

$$
S(t_1) = \left(S(0) + \int_0^{t_1} \exp\left\{ \int_0^t \Lambda\, (\beta\Theta I(u) + \mu)\, I(u) du \right\} dv \right) \exp\left\{ \int_0^t (\beta\Theta I(u) + \mu)\, du \right\}^{-1} \geq 0.
\tag{10}
$$

Therefore, $S(t)$ is non-negative for $t \geq 0$. Similar arguments establish the inequality $I(t) \geq 0$, $R(t) \geq 0$ for $t \geq 0$.
In the following, we prove the uniform boundedness of solution and obtain (7). Let

$$
N(t, x) = S(t, x) + I(t, x) + R(t, x).
\tag{11}
$$

Differentiating $N(t, x)$ with respect to time t along the solution of (4) yields

$$
\frac{\partial N(t, x)}{\partial t}\bigg|_{(4)} = \frac{\partial S(t, x)}{\partial t} + \frac{\partial I(t, x)}{\partial t} + \frac{\partial R(t, x)}{\partial t} = \varepsilon \Delta N(t, x) + \Lambda - \mu N(t, x).
$$

Then, we obtain

$$
\limsup_{t \to +\infty, x \in \Omega} (N(t, x)) = \frac{\Lambda}{\mu}.
\tag{12}
$$

Thus, it follows from Eq. (11) for any $t \geq 0$ as $S(t, x) \leq N(t, x)$, which implies that

$$\limsup_{t \to +\infty, x \in \Omega} (S(t, x)) \leq \limsup_{t \to +\infty, x \in \Omega} (N(t, x)) = \frac{\Lambda}{\mu}. \tag{13}$$

In a similar way for $I(t, x)$ and $R(t, x)$, we can get the result listed in (7).

3.2. Stability analysis of equilibrium points

According to the nullclines of non-diffusion system $\frac{dS(t)}{dt} = 0$, $\frac{dI(t)}{dt} = 0$ and $\frac{dR(t)}{dt} = 0$, and the intersection of these curves in phase space, some easy computations can show that the system (4) has two equilibrium points:

(i) Disease-free equilibrium point $E_1 = (\frac{\Lambda}{\mu}, 0, 0)$, which is the only meaningful equilibrium point in network biology if the basic reproduction number $\mathcal{R}_0 = \frac{\Lambda \beta \Theta}{\mu(\mu + \gamma)} < 1$.

(ii) Disease-spreading equilibrium point $E_2 = (S^*, I^*, R^*)$, where $S^* = \frac{\gamma + \mu}{\beta \Theta}$, $I^* = \frac{\Lambda}{\gamma + \mu} - \frac{\mu}{\beta \Theta}$, $R^* = \frac{\gamma}{\mu} I^*$, which is another meaningful equilibrium point in network biology if $\mathcal{R}_0 > 1$.

In the following, we will discuss the stability behavior of equilibrium points E_1, E_2 by the linearization technique and the Lyapunov function method [9,40,41]. Let $\tilde{S} = S - S^*$, $\tilde{I} = I - I^*$, $\tilde{R} = R - R^*$, and then drop bars for the simplicity of notations. Then system (4) can be transformed into the following form:

$$\begin{cases} \dfrac{\partial S(t, x)}{\partial t} = \varepsilon \Delta S(t, x) - \mu S(t, x) - \beta \Theta I^* S(t, x) - \beta \Theta S^* I(t, x) - \beta \Theta S(t, x) I(t, x) \\ \dfrac{\partial I(t, x)}{\partial t} = \varepsilon \Delta I(t, x) + \beta \Theta I^* S(t, x) + \beta \Theta S^* I(t, x) + \beta \Theta S(t, x) I(t, x) - \gamma I(t, x) - \mu I(t, x) \\ \dfrac{\partial R(t, x)}{\partial t} = \varepsilon \Delta R(t, x) + \gamma I(t, x) - \mu R(t, x). \end{cases} \tag{14}$$

Hence, the arbitrary equilibrium point (S^*, I^*, R^*) of system (4) can be transformed into the zero equilibrium point $(0, 0, 0)$ of system (14).

In order to further analyze the local threshold dynamics of E_1, E_2 of system (4), we will discuss the locally asymptotic stability of the zero equilibrium point of system (14). For simplicity, we choose $\Omega = [0, \pi]$.

Denote $U(t) = (u_1(t), u_2(t), u_3(t))^T = (S(t, \cdot), I(t, \cdot), R(t, \cdot))^T$, then (14) can be rewritten as an abstract ordinary differential equation in the phase space $\mathcal{C} = C([0, t], X)$ of the form

$$\dot{U} = D\Delta U(t) + L(U_t) + f(U_t), \tag{15}$$

where $D = \text{diag}\{\varepsilon, \varepsilon, \varepsilon\}$, $L : \mathcal{C} \to X$ and $f : \mathcal{C} \to X$ are given, respectively, by

$$L(\varphi) = \begin{pmatrix} -(\mu + \beta \Theta I^*)\varphi_1(0) - \beta \Theta S^* \varphi_2(0) \\ \beta \Theta I^* \varphi_1(0) + (\beta \Theta S^* - \gamma - \mu)\varphi_2(0) \\ \gamma \varphi_2(0) - \mu \varphi_3(0) \end{pmatrix} \tag{16}$$

and

$$f(\varphi) = \begin{pmatrix} -\beta \Theta \varphi_1(0)\varphi_2(0) \\ \beta \Theta \varphi_1(0)\varphi_2(0) \\ 0 \end{pmatrix}. \tag{17}$$

For $\varphi(\xi) = U_t(\xi)$, $\varphi = (\varphi_1, \varphi_2, \varphi_3)^T \in \mathcal{C}$, the linear equation of (15) at the zero equilibrium point is

$$\dot{U} = D\Delta U(t) + L(U_t), \tag{18}$$

whose characteristic equation is

$$\lambda y - D\Delta y - L(e^{\lambda \cdot} y) = 0, \tag{19}$$

where $y \in dom(\Delta)$ and $y \neq 0$, $dom(\Delta) \subset X$.

It is known that the Laplacian operator Δ on X has the eigenvalues $-k^2 (k \in N_0 \triangleq \{0, 1, 2 \ldots\})$ and corresponding eigenfunctions are

$$e_k^1 = \begin{pmatrix} \varsigma_k \\ 0 \\ 0 \end{pmatrix}, e_k^2 = \begin{pmatrix} 0 \\ \varsigma_k \\ 0 \end{pmatrix}, e_k^3 = \begin{pmatrix} 0 \\ 0 \\ \varsigma_k \end{pmatrix}, \varsigma_k = \cos(kx). \tag{20}$$

Clearly, $(e_k^1, e_k^2, e_k^3)_0^\infty$ construct a basis of the phase space X. Thus, any element y in X can be expanded as Fourier series in the following form:

$$y = \sum_{k=0}^\infty Y_k^T \begin{pmatrix} e_k^1 \\ e_k^2 \\ e_k^3 \end{pmatrix}, \quad Y_k = \begin{pmatrix} \langle y, e_k^1 \rangle \\ \langle y, e_k^2 \rangle \\ \langle y, e_k^3 \rangle \end{pmatrix}. \tag{21}$$

By calculation

$$L\left(\varphi^T \left(e_k^1, e_k^2, e_k^3\right)^T\right) = L^T(\varphi)\left(e_k^1, e_k^2, e_k^3\right), \quad k \in N_0. \tag{22}$$

According to (20) and (21), (19) is equivalent to

$$\sum_{k=0}^{\infty} Y_k^T \left[\lambda I_3 + Dk^2 - \begin{pmatrix} -(\mu + \beta\Theta I^*) & -\beta\Theta S^* & 0 \\ \beta\Theta I^* & \beta\Theta S^* - \gamma - \mu & 0 \\ 0 & \gamma & -\mu \end{pmatrix}\right] \begin{pmatrix} e_k^1 \\ e_k^2 \\ e_k^3 \end{pmatrix} = 0. \tag{23}$$

Thus, the eigenvalue equation is

$$\begin{vmatrix} \lambda + \varepsilon k^2 + \mu + \beta\Theta I^* & \beta\Theta S^* & 0 \\ -\beta\Theta I^* & \lambda + \varepsilon k^2 - \beta\Theta S^* + \gamma + \mu & 0 \\ 0 & -\gamma & \lambda + \varepsilon k^2 + \mu \end{vmatrix} = 0. \tag{24}$$

Remark 1. Since the time-dependent intervention function $\Theta(t, t_c)$ determines the system type, we next discuss separately the stability of the autonomous dynamical system without human intervention (i.e., $\Theta(t, t_c) = 1$) and the stability of the non-autonomous dynamical system with human intervention (i.e., $\Theta(t, t_c) = (1 + \exp(t - \frac{t_c}{2}))^{-1}$).

3.2.1. Local stability

Theorem 2. *If $\mathcal{R}_0 < 1$, the disease-free equilibrium point E_1 of the autonomous dynamical system* (4) *with $\Theta(t, t_c) = 1$ is local asymptotically stable, otherwise unstable for $\mathcal{R}_0 > 1$.*

Proof. For the disease-free equilibrium point E_1, the characteristic equation (24) is given by

$$\left(\lambda + \varepsilon k^2 + \mu\right)^2 \left(\lambda + \varepsilon k^2 - \frac{\beta\Theta\Lambda}{\mu} + \gamma + \mu\right) = 0. \tag{25}$$

Obviously, if $\mathcal{R}_0 < 1$, all the roots of Eq. (25) have negative real parts. According to the Routh–Hurwitz stability criterion, the equilibrium point E_1 is local asymptotically stable. If $\mathcal{R}_0 > 1$, the autonomous system has a positive eigenvalue, so E_1 is unstable.

Theorem 3. *If $\mathcal{R}_0 > 1$, the disease-spreading equilibrium point E_2 of the autonomous dynamical system* (4) *with $\Theta(t, t_c) = 1$ is local asymptotically stable.*

Proof. For the disease-spreading equilibrium point E_2, the eigenvalue equation (24) has the following form:

$$\lambda^3 + A_1\lambda^2 + A_2\lambda + A_3 = 0, \tag{26}$$

where

$$\begin{cases} A_1 = 3\varepsilon k^2 + \dfrac{\beta\Theta\Lambda}{\gamma + \mu} + \mu, \\ A_2 = \varepsilon k^2\left(\varepsilon k^2 + \dfrac{\beta\Theta\Lambda}{\gamma + \mu}\right) + (\varepsilon k^2 + \mu)\left(2\varepsilon k^2 + \dfrac{\beta\Theta\Lambda}{\gamma + \mu}\right) + (\gamma + \mu)\left(\dfrac{\beta\Theta\Lambda}{\gamma + \mu} - \mu\right), \\ A_3 = \left(\varepsilon k^2 + \mu\right)\left[\varepsilon k^2\left(\varepsilon k^2 + \dfrac{\beta\Theta\Lambda}{\gamma + \mu}\right) + (\gamma + \mu)\left(\dfrac{\beta\Theta\Lambda}{\gamma + \mu} - \mu\right)\right]. \end{cases} \tag{27}$$

For $\forall k \in N_0$, $\lambda = 0$ is not a root of Eq. (26). Furthermore, when $\mathcal{R}_0 > 1$, we obtain

$$A_1 > 0, \ A_2 > 0, \ A_3 > 0,$$

and

$$\begin{aligned} A_1 A_2 - A_3 &= \left(2\varepsilon k^2 + \frac{\beta\Theta\Lambda}{\gamma + \mu}\right)\left[4\varepsilon^2 k^4 + 2\varepsilon\frac{\beta\Theta\Lambda k^2}{(\gamma + \mu)} + 4\mu\varepsilon k^2 + \frac{\beta\Theta\Lambda}{\gamma + \mu}(\gamma + 2\mu) - \gamma\mu\right] \\ &= \left(2\varepsilon k^2 + \frac{\beta\Theta\Lambda}{\gamma + \mu}\right)\left\{4\varepsilon^2 k^4 + 2\varepsilon\frac{\beta\Theta\Lambda k^2}{(\gamma + \mu)} + 4\mu\varepsilon k^2 + \gamma\mu\left[\left(1 + \frac{2\mu}{\gamma}\right)\mathcal{R}_0 - 1\right]\right\} \\ &> 0. \end{aligned}$$

According to the Routh–Hurwitz criteria, for $\mathcal{R}_0 > 1$ all the roots of Eq. (26) have negative real parts with $k = 0, 1, 2\ldots$, and the interior equilibrium point E_2 is locally asymptotically stable.

Further, we shall discuss the global stability of system as follows.

3.2.2. Global stability

Theorem 4. *The disease-free equilibrium point E_1 of the autonomous dynamical system* (4) *with $\Theta(t, t_c) = 1$ is globally asymptotically stable when $\mathscr{R}_0 < 1$ holds.*

Proof. Let $(S(t, x), I(t, x), R(t, x))$ be any positive solution of autonomous dynamical system (4) with the initial conditions (5) and the homogeneous Neumann boundary conditions (6).

We consider the following Lyapunov functional:

$$L_1 = \int_\Omega \left[S(t, x) - \frac{\Lambda}{\mu} - \frac{\Lambda}{\mu} \ln \frac{\mu S(t, x)}{\Lambda} + I(t, x) \right] dx. \tag{28}$$

Calculating the time derivative of L_1 along the positive solution of system (4), we obtain

$$
\begin{aligned}
\frac{dL_1}{dt}\bigg|_{(4)} &= \int_\Omega \left[\left(1 - \frac{\Lambda}{\mu S(t, x)} \right) \frac{\partial S(t, x)}{\partial t} + \frac{\partial I(t, x)}{\partial t} \right] dx \\
&= \int_\Omega \left[\left(1 - \frac{\Lambda}{\mu S(t, x)} \right)(\Lambda - \mu S(t, x) - \gamma I(t, x) - \mu I(t, x)) + \left(1 - \frac{\Lambda}{\mu S(t, x)} \right) \varepsilon \Delta S(t, x) + \varepsilon \Delta I(t, x) \right] dx \\
&= \int_\Omega \left[-\frac{(\mu S(t, x) - \Lambda)^2}{\mu S(t, x)} + \frac{\Lambda \beta \Theta}{\mu} I(t, x) - (\mu + \gamma) I(t, x) + \varepsilon \Delta S(t, x) - \frac{\Lambda \varepsilon}{\mu S(t, x)} \Delta S(t, x) + \varepsilon \Delta I(t, x) \right] dx \\
&= \int_\Omega \left[-\frac{(\mu S(t, x) - \Lambda)^2}{\mu S(t, x)} + (\mu + \gamma) I(t, x)(\mathscr{R}_0 - 1) \right] dx + \varepsilon \int_\Omega \Delta S(t, x) dx - \frac{\Lambda \varepsilon}{\mu} \int_\Omega \frac{1}{S(t, x)} \Delta S(t, x) dx \\
&\quad + \varepsilon \int_\Omega \Delta I(t, x) dx.
\end{aligned}
$$

Furthermore, according to the divergence theorem and the homogeneous Neumann boundary conditions (6), we have

$$\int_\Omega \Delta S(t, x) dx = \int_{\partial\Omega} \frac{\partial S(t, x)}{\partial n} dx = 0, \quad \int_\Omega \Delta I(t, x) dx = \int_{\partial\Omega} \frac{\partial I(t, x)}{\partial n} dx = 0,$$

and

$$0 = \int_{\partial\Omega} \frac{1}{S(t, x)} \nabla S(t, x) \cdot n dx = \int_\Omega \operatorname{div}\left(\frac{1}{S(t, x)} \nabla S(t, x) \right) dx = \int_\Omega \left(\frac{1}{S(t, x)} \Delta S(t, x) - \frac{\|\nabla S(t, x)\|^2}{S^2(t, x)} \right) dx.$$

Thus,

$$\int_\Omega \frac{1}{S(t, x)} \Delta S(t, x) dx = \int_\Omega \frac{\|\nabla S(t, x)\|^2}{S^2(t, x)} dx \geq 0.$$

Now, we can further calculate $\frac{dL_1}{dt}\big|_{(4)}$, that is,

$$\frac{dL_1}{dt}\bigg|_{(4)} = \int_\Omega \left[-\frac{(\mu S(t, x) - \Lambda)^2}{\mu S(t, x)} + (\mu + \gamma) I(t, x)(\mathscr{R}_0 - 1) \right] dx - \frac{\Lambda \varepsilon}{\mu} \int_\Omega \frac{\|\nabla S(t, x)\|^2}{S^2(t, x)} dx.$$

When $\mathscr{R}_0 < 1$, we have $\frac{dL_1}{dt}\big|_{(4)} \leq 0$. Obviously, the equality holds only for $S = \frac{\Lambda}{\mu}, I = 0, R = 0$. Therefore, by applying LaSalle's invariance principle, the disease-free equilibrium point E_1 is globally asymptotically stable.

Theorem 5. *If $\mathscr{R}_0 > 1$, the disease-spreading equilibrium point E_2 of the autonomous dynamical system* (4) *with $\Theta(t, t_c) = 1$ is globally asymptotically stable.*

Proof. Define a Lyapunov function as follows:

$$L_2 = \int_\Omega \left[S(t, x) - S^* - S^* \ln \frac{S(t, x)}{S^*} + I(t, x) - I^* - I^* \ln \frac{I(t, x)}{I^*} \right] dx, \tag{29}$$

where

$$S^* = \frac{\gamma + \mu}{\beta \Theta}, \ I^* = \frac{\Lambda}{\gamma + \mu} - \frac{\mu}{\beta \Theta}.$$

In the following calculation, we will use the equilibrium equations

$$\Lambda - \beta \Theta S^* I^* - \mu S^* = 0,$$
$$\beta \Theta S^* I^* = (\gamma + \mu) I^*.$$

Calculating the derivative of L_2 along positive solutions of system (4), we obtain

$$
\begin{aligned}
\left.\frac{dL_2}{dt}\right|_{(4)} &= \int_\Omega \left[\left(1 - \frac{S^*}{S(t,x)}\right)\frac{\partial S(t,x)}{\partial t} + \left(1 - \frac{I^*}{I(t,x)}\right)\frac{\partial I(t,x)}{\partial t}\right]dx \\
&= \int_\Omega \Big[(1 - \frac{S^*}{S(t,x)})(\Lambda - \beta\Theta S(t,x)I(t,x) - \mu S(t,x)) + \left(1 - \frac{I^*}{I(t,x)}\right)(\beta\Theta S(t,x)I(t,x) \\
&\quad - (\gamma + \mu)I(t,x)) + \varepsilon\left(1 - \frac{S^*}{S(t,x)}\right)\Delta S(t,x) + \varepsilon\left(1 - \frac{I^*}{I(t,x)}\right)\Delta I(t,x)\Big]dx \\
&= \int_\Omega \Big[\left(1 - \frac{S^*}{S(t,x)}\right)(\mu S^* - \mu S(t,x) + \beta\Theta S^* I^* - \beta\Theta S(t,x)I(t,x)) + \beta\Theta S(t,x)I(t,x) - \beta\Theta S^* I(t,x) \\
&\quad - \beta\Theta S(t,x)I^* + \beta\Theta S^* I^* + \varepsilon\left(1 - \frac{S^*}{S(t,x)}\right)\Delta S(t,x) + \varepsilon\left(1 - \frac{I^*}{I(t,x)}\right)\Delta I(t,x)\Big]dx \\
&= \int_\Omega \Big[-\frac{\mu(S(t,x) - S^*)^2}{S(t,x)} - \beta\Theta S^* I^*\left(\frac{S^*}{S(t,x)} - 1 - \ln\frac{S^*}{S(t,x)}\right) - \beta\Theta S(t,x)I^* + \beta\Theta S^* I^* \\
&\quad - \beta\Theta S^* I^* \ln\frac{S^*}{S(t,x)} + \varepsilon\left(1 - \frac{S^*}{S(t,x)}\right)\Delta S(t,x) + \varepsilon\left(1 - \frac{I^*}{I(t,x)}\right)\Delta I(t,x)\Big]dx \\
&= \int_\Omega \Big[-\frac{\mu(S(t,x) - S^*)^2}{S(t,x)} - \beta\Theta S^* I^*\left(\frac{S^*}{S(t,x)} - 1 - \ln\frac{S^*}{S(t,x)}\right) - \beta\Theta S^* I^*\left(\frac{S(t,x)}{S^*} - 1 - \ln\frac{S(t,x)}{S^*}\right) \\
&\quad + \varepsilon\left(1 - \frac{S^*}{S(t,x)}\right)\Delta S(t,x) + \varepsilon\left(1 - \frac{I^*}{I(t,x)}\right)\Delta I(t,x)\Big]dx.
\end{aligned}
$$

Note that the function

$$
g(\omega) = \omega - 1 - \ln\omega \geq 0 \quad (\omega > 0), \tag{30}
$$

thus we derive

$$
g\left(\frac{S^*}{S(t,x)}\right) \geq 0, \; g\left(\frac{S(t,x)}{S^*}\right) \geq 0.
$$

Similar to the proof of Theorem 4, by the divergence theorem and the homogeneous Neumann boundary conditions (6), we have

$$
\int_\Omega \left[\varepsilon\left(1 - \frac{S^*}{S(t,x)}\right)\Delta S(t,x) + \varepsilon\left(1 - \frac{I^*}{I(t,x)}\right)\Delta I(t,x)\right]dx = -\varepsilon S^* \int_\Omega \frac{\|\nabla S(t,x)\|^2}{S^2(t,x)}dx - \varepsilon I^* \int_\Omega \frac{\|\nabla I(t,x)\|^2}{I^2(t,x)}dx \leq 0.
$$

Therefore, under the condition $\mathscr{R}_0 > 1$, we have $\left.\frac{dL_2}{dt}\right|_{(4)} \leq 0$. Obviously, the largest invariant set in the set $\left.\frac{dL_2}{dt}\right|_{(4)} = 0$ is the disease-spreading equilibrium point E_2. According to LaSalle's invariance principle, the disease-spreading equilibrium point E_2 of the autonomous dynamical system (4) with $\Theta(t, t_c) = 1$ is globally asymptotically stable.

3.3. Stability analysis of non-autonomous dynamical system

Theorem 6. *For the case of time-dependent function $\Theta(t, t_c) = (1 + \exp(t - \frac{t_c}{2}))^{-1}$, the arbitrary equilibrium point $E^* = (S^*, I^*, R^*)$ of non-autonomous dynamical system (4) is uniformly stable.*

Proof. According to the positive and boundedness of the system in Theorem 1, we have

$$
\limsup_{t\to+\infty, x\in\Omega} (S(t,x) + I(t,x) + R(t,x)) = \frac{\Lambda}{\mu},
$$

and

$$
\limsup_{t\to+\infty, x\in\Omega} (S(t,x), I(t,x), R(t,x)) \leq \frac{\Lambda}{\mu}(1, 1, 1).
$$

Then, for $t > 0$, we can derive the norm of the equilibrium point $\|E(t,x)\| = \|(S(t,x), I(t,x), R(t,x))\| \leq \frac{\Lambda}{\mu}$. For $t = 0$, the norm of the initial equilibrium point $\|E(0,x)\| = \|(S(0,x), I(0,x), R(0,x))\| = \|(\frac{\Lambda}{\mu}, 0, 0)\| = \frac{\Lambda}{\mu}$.

Construct a class $\mathcal{K}$ function $v(\|E\|) = c\|E\|$, where the constant $c > \max(1, \frac{\Lambda}{\mu})$. Hence, $\forall t \geq 0$, we have $\|E(0,x)\| < c$, and $\|E(t,x)\| < v(\|E(0,t)\|) = c\|E(0,t)\|$. By applying Lemma 4.1 of Ref. [41], the arbitrary equilibrium point $E^* = (S^*, I^*, R^*)$ of non-autonomous dynamical system (4) with $\Theta(t, t_c) = (1 + \exp(t - \frac{t_c}{2}))^{-1}$ is uniformly stable.
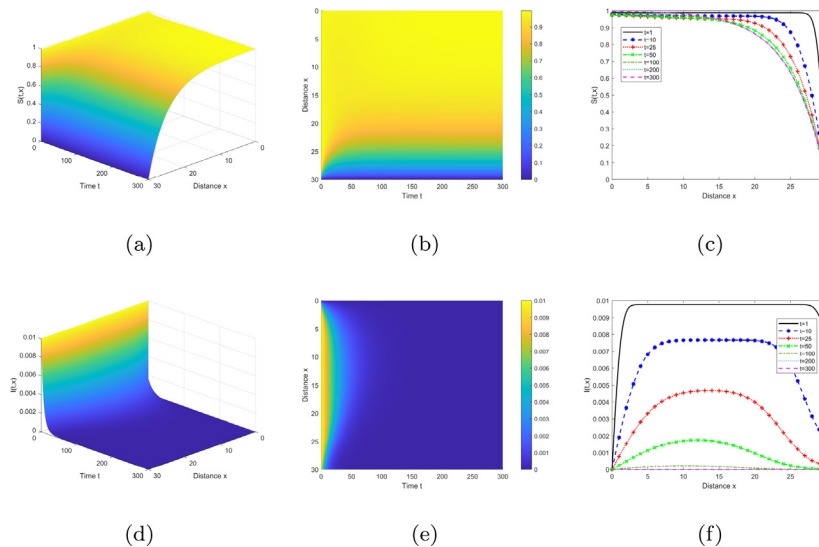
Fig. 5. The pattern formation with $\mathscr{R}_0 < 1$. Spatiotemporal evolution of susceptibles $S(t, x)$ presented in (a), (b) and (c); evolution of infectives $I(t, x)$ shown in (d), (e) and (f).

In what follows, we perform numerical results on disease spreading in continuous space and verify the correctness of the above theoretical analysis. Numerical solutions for the PDEs (4) are obtained by using the MATLAB *pdepe* function. The function solves the initial–boundary value problem with two independent variables: spatial variable and time variable. The coefficients of the equations are provided in the function handle *pdefun*, the initial values are coded in *icfun*, and the boundary conditions are coded in *bcfun*.

The *pdepe* function transforms the PDEs system into an ODEs system by spatial discretization with Petrov–Galerkin method on a set of user-defined nodes (*Xmesh*) [42]. The resulting ODEs system is integrated in time with the built-in solver *ode*15*s*. The variable time-step integration of *ode*15*s* provides numerical solutions at specific time points defined in *tspan*. The pdepe function returns the solution value based on the mesh specified by *xmesh*.

We consider the spatially continuous model (4) with homogeneous Neumann boundary conditions (6) at $x \in [0, 30]$ and the following initial conditions:

$$S(0, x) = 1 - I(0, x), \ I(0, x) = 0.01, \ R(0, x) = 0.$$

Now we give three examples on the long-time behavior of solutions of model (4).

Example 1. Let $\varepsilon = 0.5$, $\Lambda = \mu = 0.02$, $\beta = 0.3$, $\Theta = 1$ and $\gamma = 0.3$, we can get the reproduction number $\mathscr{R}_0 = 0.9375 < 1$. It follows from Theorem 4 that the disease-free equilibrium E_1 is globally asymptotically stable. As Fig. 5 shows that the density of infected individuals $I(t, x)$ converges to zero from the initial infection density over time. That is to say, in this situation the disease is not able to start spreading.

Example 2. Fix $\varepsilon = 0.5$, $\Lambda = \mu = 0.02$, $\beta = 0.3$, $\Theta = 1$ and $\gamma = 0.2$. By simple calculation, we know that the reproduction number is $\mathscr{R}_0 = 1.3636 > 1$, and the disease-spreading equilibrium point E_2 is globally asymptotically stable from Theorem 5, as shown in Fig. 6. This is to say, disease can continue spreading in new host populations.

Example 3. Fix $\varepsilon = 0.5$, $\Lambda = \mu = 0.02$, $\beta = 0.3$, $\Theta(t, t_c) = (1 + \exp(t - \frac{t_c}{2}))^{-1}$ and $\gamma = 0.2$. Here, assume that the time t_c taken to control the spread of disease is 50 day. It follows from Theorem 6 that the equilibrium of non-autonomous dynamical system is uniformly stable. From Fig. 7, we can observe that during an initial time slice with $\mathscr{R}_0 > 1$, the density of infected individuals begins to increase. Next, due to the role of the intervention function $\Theta(t, t_c)$, the reproduction number decreases to less than 1 over time, that is, the disease cannot continue spreading in new host populations and there have been no newly infected individuals on the 50th day.

4. Model prediction of COVID-19 propagation

To assess the effect of human mobility pattern with respect to the spread of COVID-19, we discuss two cases concerning human mobility network in the clustering perspective. 336 cities have been divided into 12 clusters through the high-order spectrum method (see Fig. 3). According to the derived propagation threshold and epidemiological surveys of clade
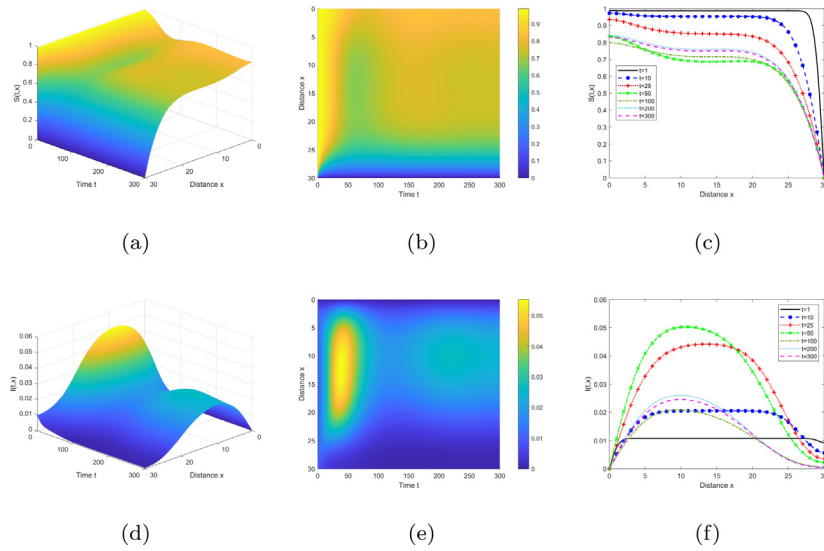
Fig. 6. The pattern formation with $\mathscr{R}_0 > 1$. Spatiotemporal evolution of susceptibles $S(t, x)$ presented in (a), (b) and (c); evolution of infectives $I(t, x)$ shown in (d), (e) and (f).
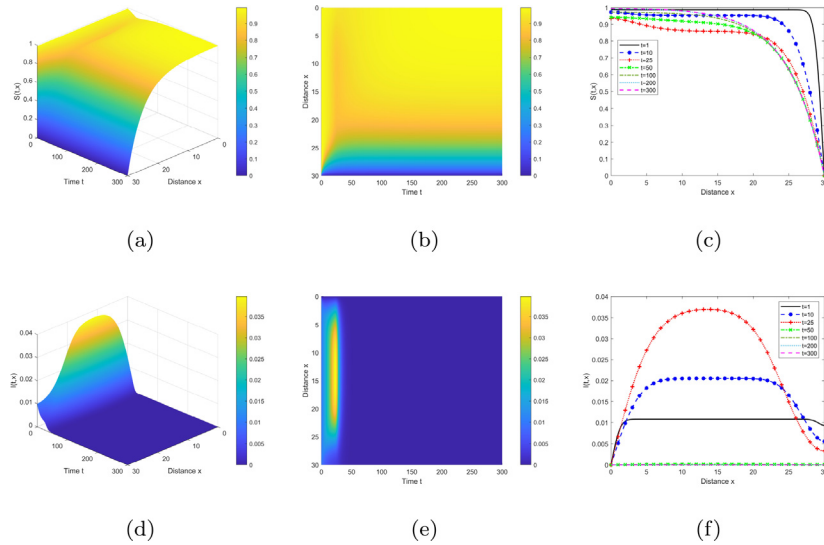

Fig. 7. The pattern formation with the time-dependent function $\Theta(t, t_c)$. Spatiotemporal evolution of susceptibles $S(t, x)$ presented in (a), (b) and (c); evolution of infectives $I(t, x)$ shown in (d), (e) and (f).

19A/19B viruses [43,44], we estimate that $\mathscr{R}_0 = 3.11$, $\gamma = 0.1\ day^{-1}$, $\beta = (\gamma + \mu)\mathscr{R}_0$ with $\Lambda = 0.00852$ and $\mu = 0.00707$ [45]. By dividing the migrant population by the total population of China, we get the average mobility rate $\varepsilon = 0.048$. Notice that the population size N_i of different cities/population $i(i = 1, 2, \ldots, 336)$ is different, so here we use the number of infections rather than the density of infections to compare infection among cities horizontally. Specifically, we multiply the resulting infection density for each city i by the population size N_i of the corresponding city to obtain the infected population for each city. Next, we will explore how the global properties (epidemic duration, peak time, and infection size) of COVID-19 correlate with the initial outbreak location (OL) and human mobility patterns in geospatial.

4.1. Without intervention

We separately choose 2 cities with average outflow (Xuzhou in Cluster 1 and Mianyang in Cluster 5) as initial outbreak locations (OLs) to start spreading. Fig. 8 depicts the spread of the epidemic between clusters and within clusters in the
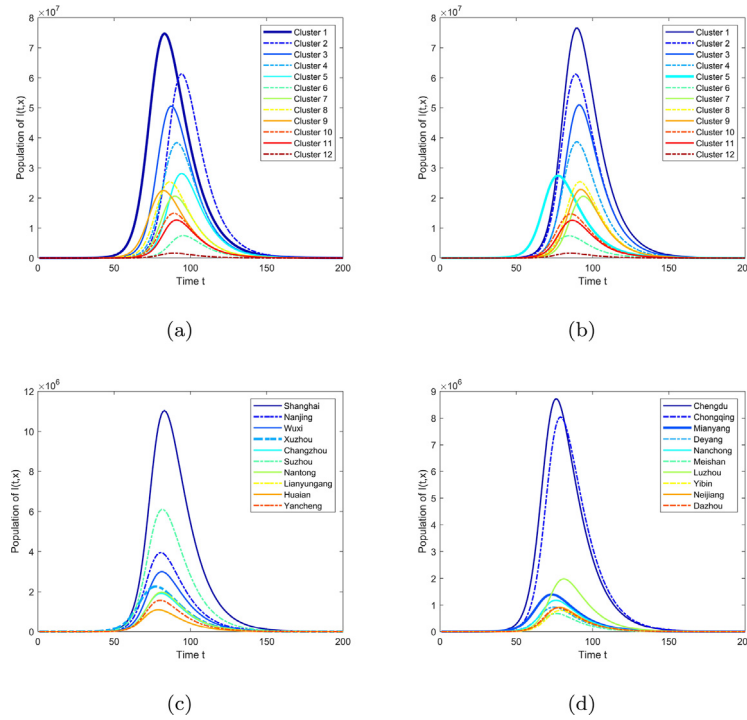
Fig. 8. Time evolution of the infected population without human intervention obtained by choosing different OLs, (a) (c) Xuzhou and (b) (d) Mianyang, respectively. The trajectories of 12 clusters are shown in (a) (b). The trajectories of the top-10 cities with population outflow in cluster 1 including Xuzhou are shown in (c) and in cluster 5 including Mianyang are shown in (d), respectively.

absence of intervention. The OL preferentially infects the particles in its cluster, which causes the outbreak of disease in that cluster first (e.g., cluster1 in Fig. 8(a) and cluster 5 in Fig. 8(b)), and then spread to the remaining clusters.

Fig. 9 presents the correlation between cumulative infected population and cluster flux for the simulation shown in Fig. 8(a), 8(b). We use the Pearson correlation coefficient r to measure the linear correlation between the cluster flux and the cumulative infected population, and $R^2 = r*r$ to measure the effect of the fit. With Xuzhou and Mianyang as the initial outbreak locations, the Pearson coefficients are 0.9632 and 0.9662, respectively. The results show two points: First, there is an almost linear relationship between cluster flux and cumulative infected population without interventions; second, this highly linear relationship does not change even if the outbreak location is different. That is, high-flux clusters induce pandemic, and independent of initial OLs. Moreover, focusing on the cities within the cluster we still find alike spreading patterns, with metropolitan regions more susceptible to disease propagation, such as Shanghai, Nanjing, Suzhou in cluster 1, and Chengdu and Chongqing in cluster 5 (see Fig. 8(c), 8(d)).

4.2. With intervention

During the pandemic of COVID-19, a series of control measures, such as wearing masks, staying one-meter apart, and injecting vaccines, are aimed at reducing the virus transmissibility among individuals as much as possible. Therefore, we introduce a time-dependent control factor into the model (2) by affecting the infection rate β of interactive items by $\beta \Theta(t, t_c)$ to simulate human intervention, where the function $\Theta(t, t_c)$ tends to 0 from 1 over time, and $t_c = 50$.

Fig. 10 illustrates the trend of infected individual $I(t, x)$ over time with intervention, which ensures that the introduction of a control factor into the model can have a profound effect on susceptible individuals. We can observe in Fig. 10(a), 10(b) that the cluster including the initial OL has a longer infection duration and larger outbreak size than other clusters. Significantly, compared with those without intervention (see Fig. 8), the infection duration is greatly shortened and the peak of epidemics decreased by three orders of magnitude in all clusters. Meanwhile, the role of metropolitan nodes has also been effectively diminished in the process of epidemic spread, and the maximum size of the outbreak only occurs at the source, as shown in Fig. 10(c), 10(d).

Fig. 11 presents the correlation between cumulative infected population and cluster flux for the simulation shown in Fig. 10(a), 10(b). The Pearson correlation coefficients r are 0.6532 and 0.0484, respectively. The results show that there is
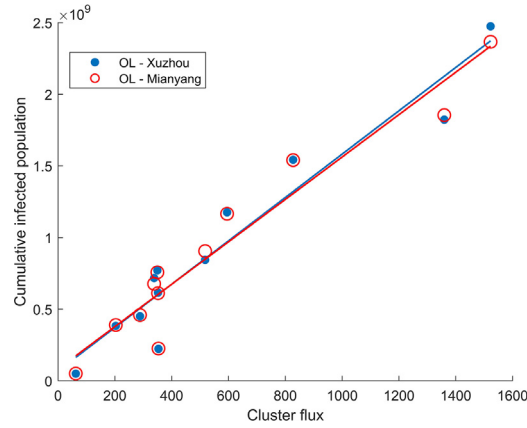
Fig. 9. The correlation between cumulative infected population and corresponding cluster flux without intervention. Clusters are represented by data points, the linear fitting of OL Xuzhou is represented by the blue line ($R^2 = 0.9278$), and the linear fitting of OL Mianyang is represented by the red line ($R^2 = 0.9336$).
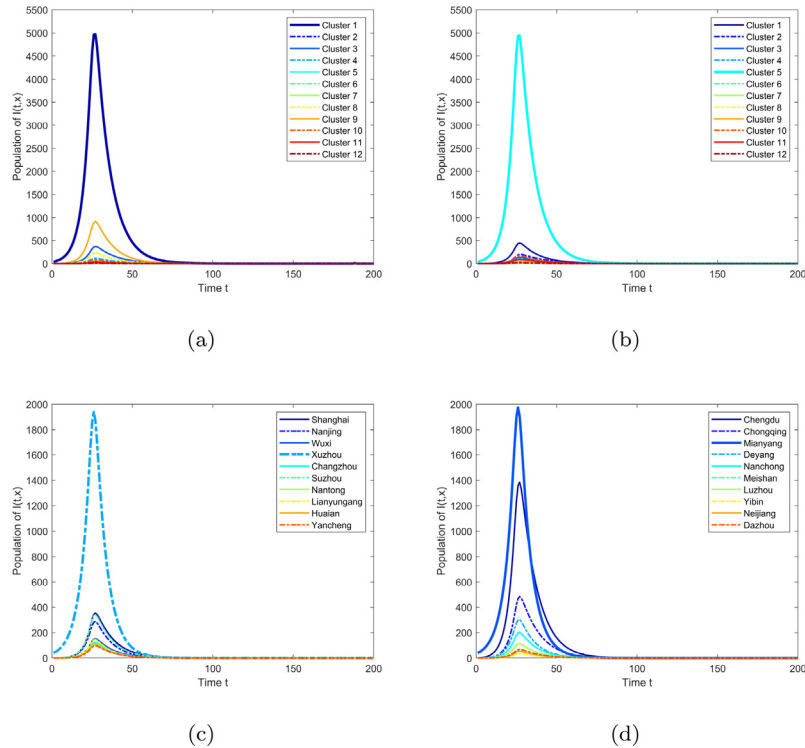

Fig. 10. Time evolution of the infected population with human intervention obtained by choosing different OLs, (a) (c) Xuzhou and (b) (d) Mianyang, respectively. The trajectories of 12 clusters are shown in (a) (b). The trajectories of the top-10 cities with population outflow in cluster 1 including Xuzhou are shown in (c) and in cluster 5 including Mianyang are shown in (d), respectively.

little correlation between the cluster flux and the number of infections. Compared to Fig. 9, this demonstrates that under the effect of human intervention, the multiscale structure of human mobility network leads to the spatial decoherence of propagation patterns.

We can observe in Fig. 12 that when the expected control time t_c increases from 30 days to 80 days, it is generally believed that the intensity of control is declining, which resulted in longer disease durations and higher infection peaks.

We simulate different scenarios of population flows by adjusting the average mobility rate ε, as shown in Fig. 13. With Xuzhou as the source of outbreak, when ε increases from 0.012 to 0.1, the infection peaks in Xuzhou will decrease, while the infection peaks in Shanghai, Nanjing and Suzhou will increase, and then change little at a certain peak. This is in line
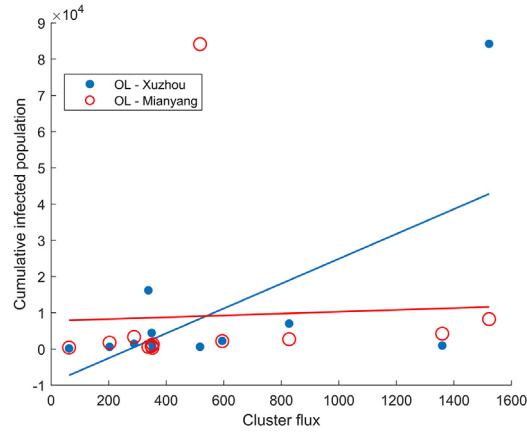
Fig. 11. The correlation between cumulative infected population and corresponding cluster flux with intervention. Clusters are represented by data points, the linear fitting of OL Xuzhou is represented by the blue line ($R^2 = 0.4266$), and the linear fitting of OL Mianyang is represented by the red line ($R^2 = 0.0023$).
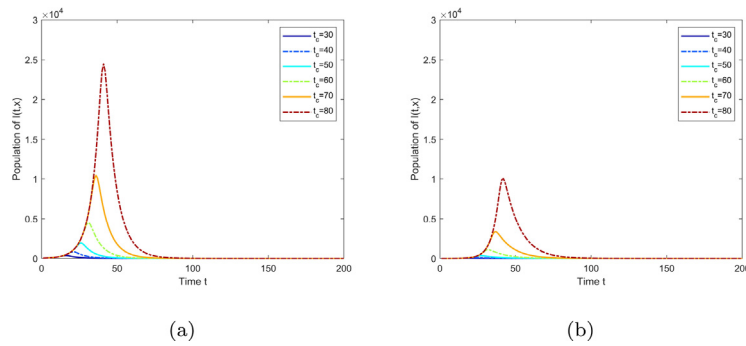

Fig. 12. Time evolution of the infected population under different t_c in Xuzhou (a) and Shanghai (b), with Xuzhou as initial outbreak location.

with Fick's second law $\frac{\partial C(t,x)}{\partial t} = D\frac{\partial^2 C(t,x)}{\partial x^2}$, and the increase in diffusion coefficient strengthens the spread from cities with high infection density to cities with low infection density.

4.3. Fitting COVID-19 data for Shanghai

To predict COVID-19 for a given period of time, we use the confirmed case data in Shanghai from March 28, 2022 to May 26, 2022 [46], and the fitting procedure is performed in Python 3.9. First, We apply the Nelder–Mead method to search for the local optimization of the parameters, and then fit the model (4) using the Levenberg–Marquardt method of least squares. In the fitting process, once the parameters are determined, we apply the fourth-order Runge–Kutta method to numerically solve the model for multi-step forward prediction in time dimension. Set the initial conditions $I(t_0) = C(t_0)/N$, $S(t_0) = 1 - I(t_0)$, where $C(t_0)$ is the number of cases at time t_0, and N is the resident population in Shanghai. To ensure the prediction accuracy, it is assumed that the recruitment rate Λ equals the death rate μ. The estimated parameters are as follows: $\beta = 0.64$, $\gamma = 0.1$, $\Lambda = \mu = 0.06$, $\varepsilon = 0.03$.

We use the case data of the first 30 days as the training set to obtain the time evolution curve of infection status, and the case data of the last 30 days as the test set for model verification, the prediction results are shown in Fig. 14. By simple calculation, the mean relative accuracy of the fit $MRA = \frac{1}{n}\sum_{t=1}^{n}(1 - \frac{|C_{actual} - C_{predict}|}{C_{actual}}) = 0.85$, where C_{actual} denotes the actual value, $C_{predict}$ is the predicted value and n is the number of sample points. The results show that the model not only reproduces the growth process of COVID-19 cases, but also has acceptable prediction performance.

5. Conclusion

This work investigates the dynamics of a reaction–diffusion epidemic model over both temporal and spatial dimensions on human mobility networks. Then, Contagion process on human mobility networks is abstractly transformed into two related processes: local growth process and regional diffusion process. Combining these two processes, a SIR-type kinetic
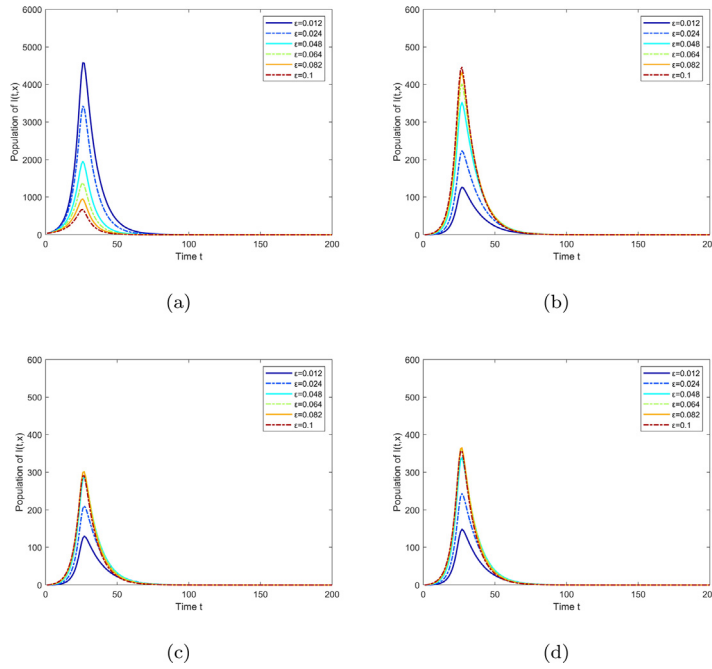
Fig. 13. Time evolution of the infected population under different ε obtained in Xuzhou (a), Shanghai (b), Nanjing (c) and Suzhou (d), with Xuzhou as initial outbreak location.
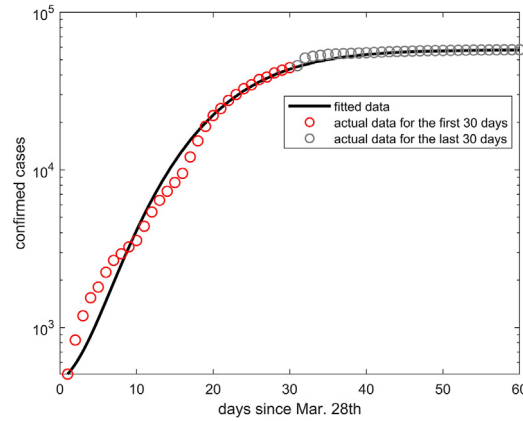

Fig. 14. Predicted versus actual cases growth in Shanghai from March 28, 2022 to May 26, 2022.

spreading model at the nodes coupled by a geographic diffusion term is presented to describe COVID-19 propagation for city clusters in China.

In the proposed model, we incorporate a time-dependent function $\Theta(t, t_c)$ to characterize human intervention. This function allows us to measure the effect of intervention to control COVID-19 by adjusting the parameter t_c. Because the time-dependent function changes the type of system, we discuss the stability of autonomous dynamical system and non-autonomous dynamical system separately, and further numerically simulate the constant and time-varying threshold behavior of the system. The results reveal that the dynamics of epidemic transmission is determined by defining the basic reproduction number $\mathscr{R}_0$.

For the human mobility network environment with spatial heterogeneity, in absence of human intervention, the simulation results demonstrate that there is an almost linear relationship between population mobility and the size of infection. Significantly, human intervention can effectively induce spatial decoherence in the process of disease transmission. Moreover, when the mobility rate between cities increases, cases in cities with high infection density will diffuse more quickly to cities with low infection density and reach a certain balance. Finally, the prediction performance of the proposed model is verified by using the actual case data in Shanghai.

In the present work, we establish a static human mobility network, which simulates different migration scenarios only by manually adjusting the average mobility rate ε. However, population mobility is generally affected by a wide range of uncertainties such as climate, festivals and epidemic prevention measures, thus future perspectives include the application of dynamic time-varying networks to assess the spread of the epidemic. Furthermore, China has always adhered to its dynamic zero-COVID policy and strategies to tackle both imported and domestic infections, so we assume that the control strategies $\Theta(t, t_c)$ in 336 cities in China are consistent. However, in addition to considering the evolution of $\Theta(t, t_c)$ over time, when focusing on different countries, the heterogeneity of control strategies over space is also an essential characteristic to describe the impact of infectious diseases. We aim to tackle these problems in future investigations.

CRediT authorship contribution statement

Ruqi Li: Data collection, Model calculation, Software, Writing – original draft. **Yurong Song:** Conceptualization, Funding acquisition, Supervision, Result analysis. **Haiyan Wang:** Methodology, Resources, Writing – review & editing. **Guo-Ping Jiang:** Research logic, Project administration, Funding acquisition. **Min Xiao:** Conceptualization, Resources, Formal analysis.

Declaration of competing interest

The authors declare that they have no known competing financial interests or personal relationships that could have appeared to influence the work reported in this paper.

Data availability

Data will be made available on request.

Acknowledgments

Appendix A. Supplementary data

Supplementary material related to this article can be found online at https://doi.org/10.1016/j.physa.2022.128337.

References

[1] S. Chen, J. Yang, W. Yang, et al., COVID-19 control in China during mass population movements at New Year, Lancet 395 (2020) 764–766, http://dx.doi.org/10.1016/S0140-6736(20)30421-9.

[2] L. Hufnagel, D. Brockmann, T. Geisel, Forecast and control of epidemics in a globalized world, Proc. Natl. Acad. Sci. USA 101 (2004) 15124–15129, http://dx.doi.org/10.1073/pnas.0308344101.

[3] M.E. Halloran, A. Vespignani, N. Bharti, et al., Ebola: mobility data, Science 346 (2014) 433, http://dx.doi.org/10.1126/science.346.6208.433-a.

[4] World Health Organization, Situation Updates–COVID-19 vaccines, Available online: https://www.who.int/emergencies/diseases/novel-coronavirus-2019/covid-19-vaccines.

[5] N.G. Davies, A.J. Kucharski, R.M. Eggo, et al., Effects of non-pharmaceutical interventions on COVID-19 cases, deaths, and demand for hospital services in the UK: a modelling study, Lancet Public Health 5 (2020) e375–e385, http://dx.doi.org/10.1016/S2468-2667(20)30133-X.

[6] L. Tian, X. Li, F. Qi, et al., Harnessing peak transmission around symptom onset for non-pharmaceutical intervention and containment of the COVID-19 pandemic, Nature Commun. 12 (2021) 1147, http://dx.doi.org/10.1038/s41467-021-21385-z.

[7] World Health Organization, Tracking SARS-CoV-2 variants, Available online: https://www.who.int/activities/tracking-SARS-CoV-2-variants.

[8] W.O. Kermack, A.G. McKendrick, A contribution to the mathematical theory of epidemics, Proc. R. Soc. Lond. Ser. A Math. Phys. Eng. Sci. 115 (1927) 700–721, http://dx.doi.org/10.1098/rspa.1927.0118.

[9] J. Wang, F. Xie, T. Kuniya, Analysis of a reaction-diffusion cholera epidemic model in a spatially heterogeneous environment, Commun. Nonlinear Sci. Numer. Simul. 80 (2020) 104951, http://dx.doi.org/10.1016/j.cnsns.2019.104951.

[10] J.T. Herbeck, J.E. Mittler, G.S. Gottlieb, et al., An HIV epidemic model based on viral load dynamics: value in assessing empirical trends in HIV virulence and community viral load, PLoS Comput. Biol. 10 (2014) e1003673, http://dx.doi.org/10.1371/journal.pcbi.1003673.

[11] A. Rizzo, B. Pedalino, M. Porfiri, A network model for Ebola spreading, J. Theoret. Biol. 394 (2016) 212–222, http://dx.doi.org/10.1016/j.jtbi.2016.01.015.

[12] Y. Huang, D. Liu, H. Wu, Hierarchical bayesian methods for estimation of parameters in a longitudinal HIV dynamic system, Biometrics 62 (2006) 413–426, http://dx.doi.org/10.1111/j.1541-0420.2005.00447.x.

[13] J. Zhang, J. Lou, Z. Ma, et al., A compartmental model for the analysis of SARS transmission patterns and outbreak control measures in China, Appl. Math. Comput. 162 (2005) 909–924, http://dx.doi.org/10.1016/j.amc.2003.12.131.

[14] S. He, S. Tang, L. Rong, et al., A discrete stochastic model of the COVID-19 outbreak: Forecast and control, Math. Biosci. Eng. 17 (2020) 2792–2804, http://dx.doi.org/10.3934/mbe.2020153.

[15] J. Jia, X. Lu, Y. Yuan, et al., Population flow drives spatio-temporal distribution of COVID-19 in China, Nature 582 (2020) 389–394, http://dx.doi.org/10.1038/s41586-020-2284-y.

[16] Z. Yang, Z. Zeng, K. Wang, et al., Modified SEIR and AI prediction of the epidemics trend of COVID-19 in China under public health interventions, J. Thorac. Dis. 12 (2020) 165–174, http://dx.doi.org/10.21037/jtd.2020.02.64.

[17] S. Wang, Y. Ding, H. Lu, S. Gong, Stability and bifurcation analysis of SIQR for the COVID-19 epidemic model with time delay, Math. Biosci. Eng. 18 (2021) 5505–5524, http://dx.doi.org/10.3934/mbe.2021278.

[18] H. Khan, F. Ahmad, O. Tunç, et al., On fractal-fractional Covid-19 mathematical model, Chaos Solitons Fractals 157 (2022) 111937, http://dx.doi.org/10.1016/j.chaos.2022.111937.

[19] R. Pascoal, H. Rocha, Population density impact on COVID-19 mortality rate: A multifractal analysis using French data, Physica A 593 (2022) 126979, http://dx.doi.org/10.1016/j.physa.2022.126979.

[20] E. Kokomo, Y. Emvudu, Mathematical analysis and numerical simulation of an age-structured model of cholera with vaccination and demographic movements, Nonlinear Anal. RWA 45 (2019) 142–156, http://dx.doi.org/10.1016/j.nonrwa.2018.06.011.

[21] J. Wang, R. Zhang, T. Kuniya, A note on dynamics of an age-of-infection cholera model, Math. Biosci. Eng. 13 (2016) 227–247, http://dx.doi.org/10.3934/mbe.2016.13.227.

[22] K. Prem, Y. Liu, T.W. Russell, et al., The effect of control strategies to reduce social mixing on outcomes of the COVID-19 epidemic in Wuhan, China: a modelling study, Lancet Public Health 5 (2020) e261–e270, http://dx.doi.org/10.1016/S2468-2667(20)30073-6.

[23] H.W. Hethcote, The mathematics of infectious diseases, SIAM Rev. 42 (2000) 599–653, http://dx.doi.org/10.1137/S0036144500371907.

[24] J. Yang, Epidemic spreading on multilayer homogeneous evolving networks, Chaos 29 (2019) 103146, http://dx.doi.org/10.1063/1.5108951.

[25] L. Feng, Q. Zhao, C. Zhou, Epidemic spreading in heterogeneous networks with recurrent mobility patterns, Phys. Rev. E 102 (2020) 022306, http://dx.doi.org/10.1103/PhysRevE.102.022306.

[26] M. del Valle Rafo, P. Aparicio, Simple epidemic network model for highly heterogeneous populations, J. Theoret. Biol. 486 (2020) 110056, http://dx.doi.org/10.1016/j.jtbi.2019.110056.

[27] T. Li, X. Liu, J. Wu, C. Wan, Z. Guan, Y. Wang, An epidemic spreading model on adaptive scale-free networks with feedback mechanism, Physica A 450 (2016) 649–656, http://dx.doi.org/10.1016/j.physa.2016.01.045.

[28] C. Liu, R. Cui, Qualitative analysis on an SIRS reaction–diffusion epidemic model with saturation infection mechanism, Nonlinear Anal. RWA 62 (2021) 103364, http://dx.doi.org/10.1016/j.nonrwa.2021.103364.

[29] W. Wang, X. Gao, Y. Cai, H. Shi, S. Fu, Turing patterns in a diffusive epidemic model with saturated infection force, J. Franklin Inst. B 355 (15) (2018) 7226–7245, http://dx.doi.org/10.1016/j.jfranklin.2018.07.014.

[30] W. Wang, Y. Cai, M. Wu, K. Wang, Z. Li, Complex dynamics of a reaction–diffusion epidemic model, Nonlinear Anal. RWA 13 (5) (2012) 2240–2258, http://dx.doi.org/10.1016/j.nonrwa.2012.01.018.

[31] H. Wang, F. Wang, K. Xu, Modeling Information Diffusion in Online Social Networks with Partial Differential Equations, Springer Cham, Berlin, Germany, 2020, http://dx.doi.org/10.1007/978-3-030-38852-2.

[32] F. Wang, H. Wang, K. Xu, et al., Characterizing information diffusion in online social networks with linear diffusive model, in: 2013 IEEE 33rd International Conference on Distributed Computing Systems, IEEE, 2013, pp. 307–316, http://dx.doi.org/10.1109/ICDCS.2013.14.

[33] R. Li, Y. Song, G.P. Jiang, Prediction of epidemics dynamics on networks with partial differential equations: A case study for COVID-19 in China, Chin. Phys. B 30 (2021) 120202, http://dx.doi.org/10.1088/1674-1056/ac2b16.

[34] National Development and Reform Commission, Data from the 2020 Spring Festival travel rush, Available online: https://www.ndrc.gov.cn/xwdt/ztzl/cyzl/2020cy/cysj/?code=&state=123.

[35] R. Milo, S. Shen-Orr, S. Itzkovitz, et al., Network motifs: simple building blocks of complex networks, Science 298 (2002) 824–827, http://dx.doi.org/10.1126/science.298.5594.824.

[36] Ö.N. Yaveroğlu, N. Malod-Dognin, D. Davis, et al., Revealing the hidden language of complex networks, Sci. Rep. 4 (2014) 4547, http://dx.doi.org/10.1038/srep04547.

[37] A.R. Benson, D.F. Gleich, J. Leskovec, Higher-order organization of complex networks, Science 353 (2016) 163–166, http://dx.doi.org/10.1126/science.aad9029.

[38] Y. Wang, K. Xu, Y. Kang, H. Wang, F. Wang, A. Avram, Regional influenza prediction with sampling twitter data and PDE model, Int. J. Environ. Res. Public Health 17 (3) (2020) 678, http://dx.doi.org/10.3390/ijerph17030678.

[39] S. Tang, Q. Yan, W. Shi, X. Wang, X. Sun, P. Yu, J. Wu, Y. Xiao, Measuring the impact of air pollution on respiratory infection risk in China, Environ. Pollut. 232 (2018) 477–486, http://dx.doi.org/10.1016/j.envpol.2017.09.071.

[40] H. Zhao, J. Yuan, X. Zhang, Stability and bifurcation analysis of reaction–diffusion neural networks with delays, Neurocomputing 147 (2015) 280–290, http://dx.doi.org/10.1016/j.neucom.2014.06.065.

[41] H.J. Marquez, Nonlinear Control Systems: Analysis and Design, John Wiley & Sons, Inc., Hoboken, New Jersey, 2003.

[42] R.D. Skeel, M. Berzins, A method for the spatial discretization of parabolic equations in one space variable, SIAM J. Sci. Stat. Comput. 11 (1) (1990) 1–32, http://dx.doi.org/10.1137/0911001.

[43] J.M. Read, J.R.E. Bridgen, D.A.T. Cummings, et al., Novel coronavirus 2019-nCoV (COVID-19): early estimation of epidemiological parameters and epidemic size estimates, Philos. Trans. R. Soc. B 376 (2021) 20200265, http://dx.doi.org/10.1098/rstb.2020.0265.

[44] S. Zhao, Q. Liu, J. Ran, et al., Preliminary estimation of the basic reproduction number of novel coronavirus (2019-nCoV) in China, from 2019 to 2020: A data-driven analysis in the early phase of the outbreak, Int. J. Infect. Dis. 92 (2020) 214–217, http://dx.doi.org/10.1016/j.ijid.2020.01.050.

[45] National Bureau of Statistics of China, 2021 china statistical yearbook, Available online: http://www.stats.gov.cn/tjsj/ndsj/2021/indexch.htm.

[46] Shanghai Municipal Health Commission, Statistics of COVID-19 cases in Shanghai, Available online: https://wsjkw.sh.gov.cn/xwfb/index.html.